Simultaneous multiplane imaging of human ovarian cancer by volume holographic imaging

Gabriel V. Orsinger
Jennifer M. Watson
Michael Gordon
Ariel C. Nymeyer
Erich E. de Leon
Johnathan W. Brownlee
Kenneth D. Hatch
Setsuko K. Chambers
Jennifer K. Barton
Raymond K. Kostuk
Marek Romanowski

Simultaneous multiplane imaging of human ovarian cancer by volume holographic imaging

Gabriel V. Orsinger,[a] Jennifer M. Watson,[a] Michael Gordon,[b] Ariel C. Nymeyer,[a] Erich E. de Leon,[b] Johnathan W. Brownlee,[b] Kenneth D. Hatch,[c] Setsuko K. Chambers,[c] Jennifer K. Barton,[a,b,d,*] Raymond K. Kostuk,[b,d] and Marek Romanowski[a]

[a]University of Arizona, Department of Biomedical Engineering, Tucson, Arizona 85719
[b]University of Arizona, Department of Optical Sciences, Tucson, Arizona 85721
[c]University of Arizona, College of Medicine, Department of Obstetrics and Gynecology, Tucson, Arizona 85724
[d]University of Arizona, Electrical and Computer Engineering Department, Tucson, Arizona 85721

Abstract. Ovarian cancer is the most deadly gynecologic cancer, a fact which is attributable to poor early detection and survival once the disease has reached advanced stages. Intraoperative laparoscopic volume holographic imaging has the potential to provide simultaneous visualization of surface and subsurface structures in ovarian tissues for improved assessment of developing ovarian cancer. In this *ex vivo* ovarian tissue study, we assembled a benchtop volume holographic imaging system (VHIS) to characterize the microarchitecture of 78 normal and 40 abnormal tissue specimens derived from ovarian, fallopian tube, uterine, and peritoneal tissues, collected from 26 patients aged 22 to 73 undergoing bilateral salpingo-oophorectomy, hysterectomy with bilateral salpingo-oophorectomy, or abdominal cytoreductive surgery. All tissues were successfully imaged with the VHIS in both reflectance- and fluorescence-modes revealing morphological features which can be used to distinguish between normal, benign abnormalities, and cancerous tissues. We present the development and successful application of VHIS for imaging human ovarian tissue. Comparison of VHIS images with corresponding histopathology allowed for qualitatively distinguishing microstructural features unique to the studied tissue type and disease state. These results motivate the development of a laparoscopic VHIS for evaluating the surface and subsurface morphological alterations in ovarian cancer pathogenesis. © *The Authors. Published by SPIE under a Creative Commons Attribution 3.0 Unported License. Distribution or reproduction of this work in whole or in part requires full attribution of the original publication, including its DOI.* [DOI: 10.1117/1.JBO.19.3.036020]

1 Introduction

With an estimated 22,240 newly diagnosed cases and 14,030 deaths in the United States in 2013,[1] ovarian cancer remains one of the most enigmatic cancers. Although the 5-year survival for patients with the disease detected at an early, localized stage is 92%, the overall 5-year survival for all women diagnosed with epithelial ovarian carcinoma is only 44% due to poor prognosis when diagnosed at a late stage. Unfortunately, 85% of ovarian cancers are detected at a more advanced stage as symptoms are easily missed until the disease has spread to other regions of the body.[1] The disparity in survival rates between early and late stage ovarian cancer is due largely to the lack of appropriate screening techniques for asymptomatic, low risk population and inadequate sensitivity and specificity of existing screening methods for high risk women.[2–4] Due to overall high mortality of ovarian cancer, women at elevated risk may be counseled to undergo prophylactic and, possibly unnecessary, oophorectomy. A sensitive, minimally invasive monitoring method could be used to preserve fertility in this subset of women.

There are two potential advantages of developing an optical imaging approach for the ovaries, fallopian tubes, and peritoneum in this context. First, women at elevated risk for the development of this disease are frequently counseled to undergo

prophylactic, salpingo-oophorectomy at an early age resulting in early surgical menopause with accompanying poor quality of life. In this case, an alternative sensitive and minimally invasive monitoring method has the potential to be impactful. Second, once early ovarian cancer is suspected in a young woman, a small subset of cases, there is the potential of preserving future reproductive capacity and endogenous hormonal function. For this group of patients, a sensitive and specific intraoperative means to detect metastatic disease to the other ovary could be helpful adjuvant to standard of care surgical staging, combined with preoperative transvaginal ultrasound with or without computed tomograpy (CT) scan.

Intraoperative optical imaging enables examination of intraperitoneal surfaces at a higher resolution than the gold standard transvaginal ultrasound due to the use of light instead of oscillating sound waves and improved access to all peritoneal surfaces. Examination of the ovary and fimbrial surfaces is of particular importance as up to 90% of ovarian cancers are epithelial carcinomas and arise from either the ovarian or fimbrial epithelium.[5–7] Traditional white-light laparoscopy provides reliable surface imaging for the detection of larger ovarian neoplasm; however, early cancer development involves microscopic alterations of tissue structure, and subsurface transformations to the ovarian stroma, indicative of a nascent tumor microenvironment.[8]

High resolution, subsurface laparoscopic optical imaging of epithelial and stromal microarchitecture could potentially reveal

*Address all correspondence to: Jennifer K. Barton, E-mail: barton@email.arizona.edu

a developing neoplasm that would otherwise be missed by a surgeon making the critical decision to either remove or leave the ovaries. To optically visualize changes in surface epithelium and the subsurface stroma in carcinomas, several optical imaging modalities have been investigated, including optical coherence tomography (OCT),[9–11] confocal microscopy,[12] multiphoton microscopy,[12–17] and reflectance spectroscopy and microscopy.[18–22] OCT provides relatively large imaging depth and high temporal resolution, however it requires scanning and image reconstruction, adding to the complexity and cost of the instrument. Confocal microlaparoscopy demonstrates high spatial resolution, but requires raster scanning, restricting the ability to image multiple depths quickly. Multiphoton microscopy, including two-photon excitation fluorescence, second-harmonic generation (SHG), and third-harmonic generation (THG), has shown promise for detecting structural and metabolic differences between normal and abnormal tissues. In particular, SHG of collagen and THG of cell nuclei can provide tissue and cell morphological information *in vivo* that would otherwise only be accessible *ex vivo* by traditional hematoxylin and eosin (H&E) staining of fixed histological tissue sections.[15–17,23,24] Although promising for visualizing early changes indicative of cancer, multiphoton imaging methods rely on raster scanning and require a complex laser source. Alternatively, multiplexed volume holographic imaging, which can be realized in a mechanically simple, robust, and inexpensive system, allows for imaging of multiple depths simultaneously.[25] Should the cost and technical challenges of *in vivo* OCT, confocal, or multiphoton imaging be overcome, adjunct volume holographic imaging for close examination of suspicious regions could be beneficial.

The volume holographic imaging system (VHIS) that we present here uses a multiplexed volume hologram and inexpensive light sources to achieve depth selectivity and background rejection. This VHIS is capable of both epireflectance and epifluorescence imaging at two imaging planes with lateral and axial resolutions of approximately 4 and 22 μm, respectively.[26] We believe this to be the first demonstration of using a multiplexed volume hologram for imaging into highly scattering tissue such as the ovary. Although traditional optical microscopy or microlaparoscopy provides high quality images from a single, in-focus object plane, holographic imaging allows simultaneous acquisition of images from multiple planes within a three-dimensional volume. The resulting images from each depth plane are displayed side-by-side on a two-dimensional (2-D) monitor.

The ability to simultaneously capture multiple reflectance or fluorescence images at depth within a volume of tissue is enabled by the multiplexed volume hologram, previously described by our group.[27–29] The hologram is recorded by exposing a photosensitive polymer, 1,9-phenanthrenequinone-doped poly(methyl methacrylate) (PQ-PMMA), to an optical interference pattern formed with coherent laser illumination. To multiplex, a separate hologram is recorded into the same region of the element that will select light from a separate depth within the tissue sample. Upon illumination of the sample, light originating from each depth is collected by the different holograms and mapped to distinct regions on the detector without overlap. If illuminated by a narrow spectral bandwidth, as from a laser, a vertical line image is formed. If instead broadband illumination is used, or if fluorescence emission from the tissue sample is generated, a continuous series of adjacent line images

are formed (along the *x*-axis) according to the Bragg matching relation,[30] producing a lateral field of view (FOV) that is proportional to the spectral bandwidth of the source. In the orthogonal direction (*y*-axis), spectral Bragg matching condition is degenerate and the FOV is dictated by the imaging optics relation as in a conventional microscope. For the experiments presented in this paper, two images from two tissue depths are used; however, in earlier work, five depth projections were demonstrated, but it is possible to increase the number of depth projections beyond this with different system geometries.[29]

Targeted fluorescent probes that selectively bind to cancer cells over normal cells have shown promise for delineating cancer boundaries and improving outcomes of optical imaging-aided cytoreductive surgeries.[31,32] We have previously demonstrated fluorescence VHIS imaging using fluorescent agents that are tailored to the spectral range detectable by the VHIS.[27] In this study, we demonstrate fluorescence-mode volume holographic imaging alongside the primary reflectance-mode imaging of gynecological tissues provided by the fluorescent agents with emission spectra that fall within the same spectral range as the reflectance light source.

We examine for the first time the performance of VHIS in video-rate imaging of surface and subsurface morphologies on a wide range of human *ex vivo* ovarian tissues collected during bilateral salpingo-oophorectomy (BSO), hysterectomy with bilateral salpingo-oophorectomy (H-BSO), total abdominal hysterectomy with bilateral salpingo-oophorectomy (TAH-BSO), and debulking surgery. To complete this study, we fabricated a benchtop VHIS specifically for *ex vivo* tissue imaging; however, the system is configured for rapid adaptation into a handheld endoscope for future *in vivo* imaging studies of gynecologic tissues. Although laparoscopic screening is likely unsuitable for routine screening of average risk women, in the cases of exploratory laparotomy of symptomatic women, or screening of high risk women, laparoscopic VHIS imaging could improve the specificity when determining the necessity of prophylactic salpingo-oophorectomies, possibly reducing the unnecessary ovary removal, and therefore improving the quality of life.

2 Materials and Methods

2.1 Patients

Twenty-eight patients undergoing BSO, H-BSO, TAH-BSO, or debulking surgery at University of Arizona Medical Center—University Campus in Tucson, Arizona were asked to participate in this *ex vivo* tissue imaging study that spanned 9 months. The study was approved by the Institutional Review Board of the University of Arizona and informed consent was obtained from each patient who participated. Two consented patients were omitted from the study due to limited availability of tissue discards. From the 26 remaining patients included on this study, 118 tissue discard specimens were acquired for examination by VHIS.

2.2 Volume Holographic Imaging System

The benchtop VHIS used for this *ex vivo* tissue study was designed with a multiplexed hologram comprising two separate holograms within this single element, configured for imaging two planes in surgical biopsies, and displaying each side-by-side on the camera, as described in Fig. 1. Specific technical details on fabrication and use of multiplexed volume holographic imaging are thoroughly described in the previous works by our group and other groups.[23,26,33–40] One hologram

selects an image from the focal plane of the objective lens (similar to normal operation of a standard microscope) and the second hologram captures the defocused wavefront image originating from 50 μm above the focal plane. Each object wave was recorded with a different reference beam angle to provide side-by-side projections onto the detector—the in-focus depth image to the right half and the defocused wavefront image to the left half. The 50 μm separation between images was determined by the hologram construction parameters and the center wavelength of the reflectance light source (695 nm), and the FOV is determined by the spectral bandwidth. For this *ex vivo* tissue imaging study, the source's 55-nm bandwidth corresponded to a 160 μm FOV along the *x*-axis of the image. To enable rapid switching between reflectance and fluorescence imaging, the reflectance LED source was chosen with a central wavelength coinciding with the peak emission wavelength from the fluorescent dyes. A long-pass filter with 665 nm cut-on wavelength was used for both reflectance and fluorescence operation, acting to suppress the laser excitation in fluorescence mode.

A schematic and photograph of the benchtop VHIS are shown in Figs. 2(a) and 2(b), respectively, depicting the system's key components. The interchangeable illumination consists of either a 690 nm broadband LED (H2A1-H690, Roithner Lasertechnik GmbH, Vienna, Austria) for reflectance

imaging or a 635 nm laser diode (BWF, B&W Tek, Incorporated, Newark, Delaware) for fluorescence imaging. In either scheme, illumination light passes through a 50/50 pellicle beam splitter (BP150, Thorlabs Incorporated, Newtown, New Jersey) and then enters the 50×, 0.55 numerical aperture (NA) objective lens with a 3.64-mm focal length (ULWDMSPlan50, Olympus America Incorporated, Center Valley, Pennsylvania). A Köhler illumination configuration is used to provide uniform illumination at the sample. Optical relays are used to project the pupil to the hologram plane
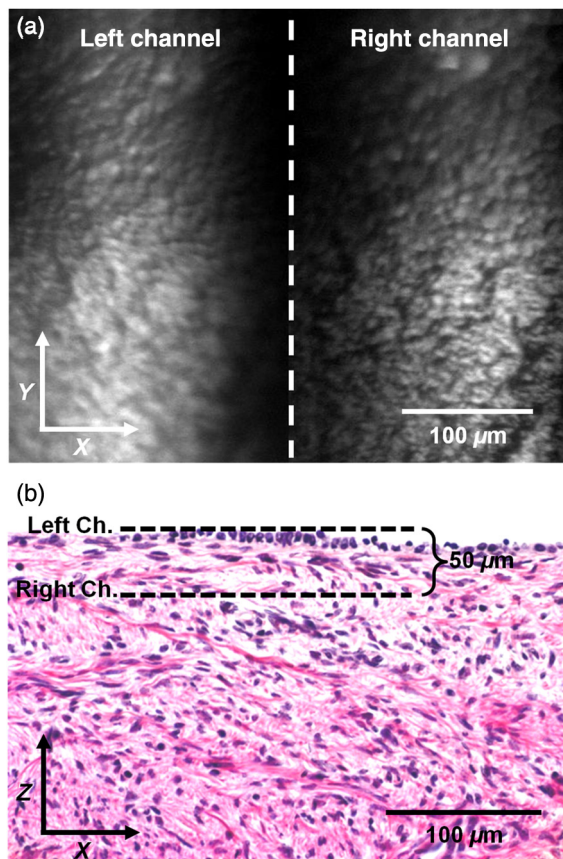

Fig. 1 (a) *En face* volume holographic imaging system (VHIS) reflectance image of normal ovarian tissue. The left channel and right channel, separated by vertical dotted line, represent the surface and subsurface image planes, respectively. (b) Cross-sectional (orthogonal plane) histology of the same tissue sample fixed and H&E stained depicting the 50 μm separation of the imaging. Scale = 100 μm, for both (a) and (b).
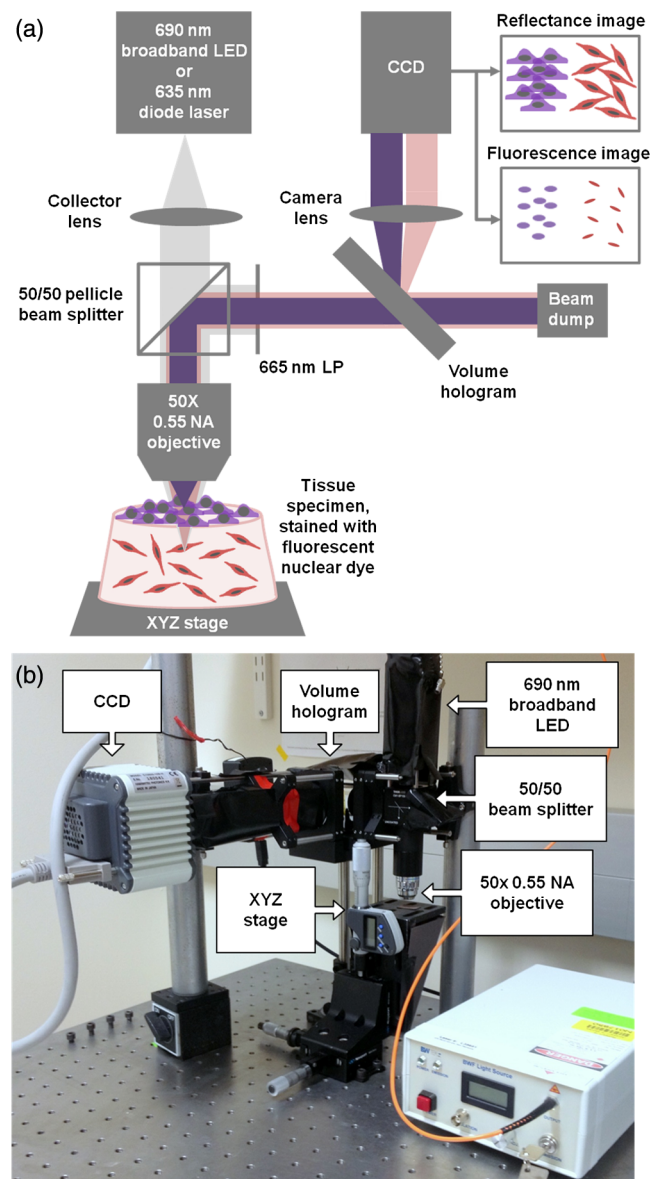

Fig. 2 (a) Schematic of the benchtop VHIS for reflectance-mode and fluorescence-mode holographic imaging of *ex vivo* tissue. In reflectance mode, light captured by the objective passes through the long-pass filter and splits into the left and right channels representing the surface and subsurface imaging planes, respectively, and projects a dual-channel image onto the CCD. In fluorescence mode, the 635 nm diode laser illuminates the sample and excites the fluorescent dye bound to cell nuclei. The fluorescence emission passes through the long-pass filter and is displayed in similar fashion to the reflectance mode. (b) Photo of the benchtop VHIS as used for *ex vivo* imaging study with key components labeled.

which prevents beam shifting and signal loss. Reflected or fluorescent light originating from the sample is captured by the objective lens, redirected by the 50/50 pellicle beam splitter, and filtered by the 665 nm long-pass filter (ET665LP, Chroma Technology Corporation, Bellows Falls, Vermont), which blocks the 635-nm excitation illumination in fluorescence mode, and reaches the multiplexed volume hologram. Here, the hologram diffracts and disperses the light along the x-axis of the image. The multiplexed gratings in the hologram are designed to select light from the tissue surface and 50 μm below the surface. The light from these two channels is focused by a camera lens (AC254-075-A, Thorlabs Incorporated, Newtown, New Jersey) and projected side-by-side onto a 1344×1024 pixels CCD camera (ORCA-R2, Hamamatsu Corporation, Middlesex, New Jersey). VHIS images were acquired using HCImage Live software (Hamamatsu Corporation, Middlesex, New Jersey). The position of the tissue specimen is adjusted using a three-axis micropositioning stage (460A Series, Newport Corporation, Irvine, California) with a digital micrometer head (DM713, Thorlabs Incorporated, Newtown, New Jersey) for z-axis control. As assembled, the VHIS provides lateral resolution of approximately 4 μm and an axial resolution of approximately 22 μm/channel. Future adaptation into a clinical endoscopic VHIS for *in vivo* imaging will be achieved by replacing the objective lens with a high NA endoscope and incorporating the hologram and all other optical components into a sealed handle for use by the oncological surgeon.

2.3 Tissue Imaging

Biopsies (approximately 125 to 1000 mm^3) were obtained from surgical discards and washed in phosphate-buffered saline (PBS) for up to 30 min following acquisition, followed by incubation in PBS containing fluorescent cellular markers for 30 min. The markers included a nuclear dye that permeates cell membranes and intercalates with deoxyribonucleic acid (HCS NuclearMask™ Deep Red Stain, Life Technologies Corporation, Grand Island, New York), and/or a membrane dye that selectively labels lipid bilayers (Vybrant® DiD Cell Labeling Solution, Life Technologies Corporation, Grand Island, New York). The peak excitation and emission wavelengths for the dyes were around 640 and 670 nm, respectively. These dyes were selected because of their emission spectra falling within the 665 to 720 nm designed dispersive axis of the VHIS. Specimens were briefly rinsed in PBS to remove excess dye prior to careful placement in a Petri dish for handling, ensuring exposure of the epithelial surface. To image with the VHIS, the sample was placed on the sample stage and brought into focus by adjusting the position of the stage in relation to the objective lens. To prevent drying, samples were hydrated with PBS while imaging.

With the broadband LED illuminating the sample, reflectance images were acquired with the CCD camera set to 2×2 pixels binning for a final image dimension of 672×512 pixels. This allowed for continuous image acquisition at 10 to 20 frames/s for 30 to 120 s while translating the stage laterally to scan a large area of the tissue specimen, mimicking conditions that would be used for *in vivo* laparoscopic imaging. For fluorescence-mode imaging, the illumination source was changed to the 635 nm laser diode and the camera was set to 4×4 pixels binning for a final image dimension of 336×256 pixels, allowing image acquisition at up to 10 frames/s, similarly for 30 to 120 s. For the binned images,

the apparent pixel size as mapped to object space is 0.63 μm for 2×2 binning, and 1.25 μm for 4×4 binning, both of which are below the system lateral resolution of 2 to 4 μm as imposed by the hologram. All image data were saved as multipage, 16-bit tagged image file format (TIFF) files and examined alongside histological micrographs from corresponding tissue sections. All tissues were imaged within 120 min of excision.

2.4 Histology and Pathological Evaluation

Immediately following VHIS imaging, tissues specimens were affixed to filter paper to maintain orientation and submerged in fixation media (HistoChoice®, Sigma-Aldrich, Incorporated, St. Louis, Missouri). Fixed tissues were dehydrated in ethanol, embedded in paraffin wax, microtome sectioned at 5 μm, and prepared on slides. Tissue specimen orientation was maintained so the resulting slides produced cross sectional views of the samples, i.e., perpendicular to the *en face* VHIS image plane. Slides were H&E stained in preparation for pathological evaluation. Histological specimens were interpreted by a pathologist independent of patient diagnosis.

2.5 Image Processing

Raw VHIS images were processed to equalize contrast and brightness variation of the left and right channels, as shown in Fig. 3. In this method, raw TIFF images, i.e., 2-D intensity matrices, were split into left and right submatrices with equal FOV. For each channel matrix, background signal was removed by subtracting the minimum intensity value of the matrix from each pixel within that matrix. This sets the minimum intensity value of both the left and right matrices to zero, represented as Image_L and Image_R, respectively. The deeper imaging plane, Image_R, consistently provided a dimmer signal as compared to Image_L. To equalize the intensity histograms of the channels, the right channel matrix was multiplied by a scalar equivalent to the ratio of Range_L over Range_R, the intensity ranges of Image_L and Image_R, as follows:

$$\text{New}_R = \left(\frac{\text{Range}_L}{\text{Range}_R}\right)(\text{Image}_R),$$

where New_R is the new, equalized 2-D right channel matrix. Finally, New_R is rejoined with Image_L to form the intensity
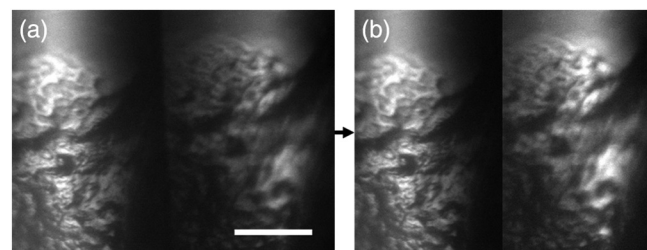

Fig. 3 Raw and processed VHIS reflectance images. Due to intensity mismatch and field of view differences between the two channels, the dimmer right channel (subsurface image) was scaled to match the range of gray levels of the brighter left channel (surface image) and both channels were cropped to result in equal footprints. (a) Raw image of an ovarian serous carcinoma specimen acquired on the VHIS. (b) The same image after cropping and intensity equalization. Scale bar = 100 μm, both images.

equalized VHIS image. For display in publication, image intensity ranges were adjusted to 5% to 95% of the gray level range.

3 Results

One hundred and eighteen tissue specimens from 26 patients (ages: 22 to 73 years, average: 49.5 years, median: 47 years) were successfully imaged with the VHIS in both reflectance and fluorescence modes. More than 70,000 reflectance-mode images and 35,000 fluorescence-mode images were acquired in total. Between one and nine tissue specimens originating from ovarian, uterine, fallopian, and/or peritoneal tissues were acquired from each patient and individually imaged following excision. Of these specimens, 64 samples originated from the ovary, 39 from the fallopian tube, five from the ovarian cancer metastases within the peritoneum, and 10 from the uterus. At the time of surgery, seven patients were classified as high risk and received prophylactic surgeries, four were diagnosed with ovarian cancer, and 15 with benign ovarian neoplasms or conditions. In most cases, both normal and abnormal tissue specimens were acquired from a single patient. Table 1 summarizes the imaged tissue specimens grouped by pathological findings.

Table 1 Summary of tissues imaged.

Tissue pathology	Patients	Tissue specimens
Ovary	25	64
Normal ovary	19	39
Normal ovary, stripped epithelium	3	5
Ovarian serous adenocarcinoma	4	10
Ovarian mucinous adenocarcinoma	1	1
Benign mucinous cystadenoma	2	5
Benign serous cystadenoma	1	1
Simple ovarian cyst	2	3
Fallopian tube	23	39
Normal fallopian tube	15	23
Normal fallopian tube, stripped epithelium	3	4
Chronic salpingitis	7	11
Fallopian tube serous adenocarcinoma	1	1
Uterus	7	10
Normal endometrium	3	3
Normal myometrium	4	4
Endometrial adenocarcinoma	2	3
Other	4	5
Metastases derived from ovarian cancer	3	4
Endometriosis of the bowel	1	1

The primary focus of the study was to assess the reflectance-mode performance of the VHIS for imaging ovarian tissues. Therefore, reflectance and fluorescent images were analyzed separately. Analysis was qualitative in nature to identify distinguishing morphological features between diagnostic categories.

For the ovarian tissues, the predominant tissue specimen groups examined by VHIS were normal ovary (39) and ovarian serous adenocarcinoma (10). Other, less commonly observed ovarian abnormalities included ovarian mucinous adenocarcinoma (1), benign mucinous cystadenoma (5), benign serous cystadenoma (1), and simple ovarian cysts (3). Additionally, four ovarian cancer metastases to the peritoneum were imaged. In consideration of experimental observations indicating that ovarian serous adenocarcinoma commonly arises from the fimbriated end of the fallopian tube for women at high risk,[5,41,42] we also examined 39 tissue specimens originating from fallopian tube in this study, of which only one was cancerous (fallopian tube serous adenocarcinoma). Ten uterine tissue specimens were also collected and imaged in this tissue study, including three normal endometrium, four normal myometrium, and three endometrial adenocarcinoma.

As stated previously, the goal of this study was to extract common features observable in VHIS images within each tissue group that can be linked to their diagnosis. Features typically identified to diagnose tissue specimens in H&E-stained histological slides were the basis for these observations; however, VHIS is a vastly different modality than typical histology. Primarily, contrast in VHIS reflectance images is provided by variations in scattering and absorption of the illumination light within the tissue, revealing morphological information. Instead, H&E-stained slides provide contrast from the chromophores H&E to highlight cellular and tissue structures to inform diagnosis. Additionally, VHIS imaging is performed *en face* at two depths, while histological slides are prepared from cross-sectional slices perpendicular to the VHIS imaging plane. In all subsequent example VHIS images, the left and right channels correspond to the surface and subsurface planes, respectively.

3.1 Normal Ovary

VHIS images of normal, epithelialized ovary showed very consistent features. Regular, cobblestone appearance of the surface, or left channel image, was observed in these normal ovarian tissues as demonstrated in Fig. 4(c), consistent with a monolayer of cuboidal epithelium, as confirmed by histology in Fig. 4(a). The subsurface or right channel of the normal ovarian tissue [Fig. 4(c)], which imaged a plane within the stroma, commonly showed a repeating wavy pattern corresponding to the regularity of the dense, Type I stromal collagen, also confirmed by histology [Fig. 4(a)]. The regular cobblestone-like pattern was also observed in the fluorescence images [Fig. 4(e)], but most fluorescent signal was consistently observed in the right or stromal channel due to the configuration of the camera in the imaging system. In five instances of normal ovarian tissue, the cobblestone epithelium was lost, resulting in flat and featureless VHIS images. Histology revealed that these ovaries were de-epithelialized peri- or postoperatively, likely due to handling.

3.2 Ovarian Serous Adenocarcinoma

Ovarian serous adenocarcinoma, the most common ovarian cancer, is characterized by well-formed papillae, abnormally large epithelial cells with large nuclei arranged in a disordered
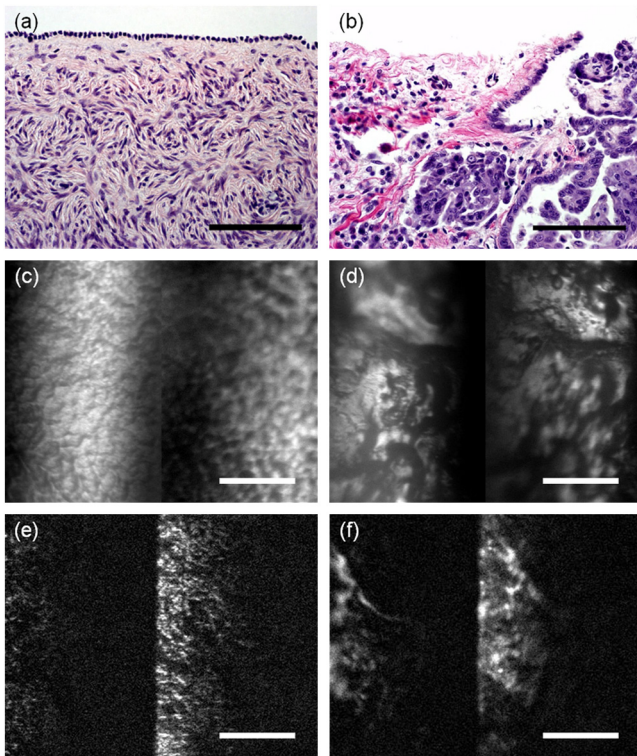
Fig. 4 VHIS images of ovarian tissues. This panel of images shows cross-sectional H&E-stained histology (a, b), *en face* reflectance-mode VHIS (c, d), and *en face* fluorescence-mode VHIS (e, f) images of normal ovary (left column) and ovarian serous adenocarcinoma (right column). VHIS image orientation is orthogonal to the histology orientation. For all VHIS images, the left half is the surface image and the right half is the subsurface image. Scale bar = 100 μm, all images.

pattern that have invaded the stroma. Morphological heterogeneity is commonly observed in ovarian serous adenocarcinoma with high variability in nuclear size. All of these features were easily identifiable in histology as depicted in Fig. 4(b). Reflectance-mode VHIS images of ovarian serous adenocarcinoma similarly showed a stark divergence from the normal ovarian images, as seen in Fig. 4(d). Both surface and subsurface imaging channels showed topographical features of irregular and variable pits and valleys consistent with histology. Fluorescence-mode images of ovarian serous adenocarcinoma [Fig. 4(f)] revealed a larger and irregular nuclei and membrane staining than those seen in normal ovarian tissues, again consistent with histology.

3.3 Mucinous Adenocarcinoma

Ovarian mucinous adenocarcinoma is less common than its serous counterpart and is characterized by disorderly stromal invasion, nuclear atypia, and mucin producing as seen in histology [Fig. 5(a)]. VHIS reflectance-mode images [Fig. 5(e)] show distinct morphological differences from the normal ovarian tissue at both surface and subsurface depths with a poorly organized structure. Fluorescence-mode images [Fig. 5(i)] also show this irregular organization of mucinous adenocarcinoma.

3.4 Mucinous Cystadenoma

Mucinous cystadenoma, a benign abnormality, is identified by one or more cystic tumors filled with mucinous fluid lined by

tall columnar epithelial cells, as seen in histology in Fig. 5(b). Corresponding reflectance- and fluorescence-mode VHIS images are shown in Figs. 5(f) and 5(j), respectively. Although columnar epithelium is difficult to identify in the VHIS images, the reflectance and fluorescence observed are neither as regular as normal ovarian epithelium nor as irregular as ovarian serous adenocarcinoma in appearance.

3.5 Serous Cystadenoma

Serous cystadenoma, also a benign abnormality, is classified by papillary architecture and moderate nuclear atypia, apparent in histology in Fig. 5(c). Unlike serous adenocarcinoma, serous cystadenoma does not exhibit stromal invasion. Corresponding reflectance- and fluorescence-mode VHIS images are shown in Figs. 5(g) and 5(k), respectively. The reflectance and fluorescence images show larger punctuate features that span both surface and subsurface channels and may correlate to the typical papillary nature of serous cystadenoma.

3.6 Metastases to the Peritoneum

Extraovarian peritoneal metastases derived from primary ovarian carcinoma exhibit microarchitectural features including tufting, nuclear atypia, and micropapillae, as seen in histology in Fig. 5(d). Reflectance-mode VHIS image of a metastasis biopsy is shown in Fig. 5(h) and exhibits a smooth background appearance in both channels with an irregular pattern of punctuate surface features. Similarly in the fluorescence-mode image [Fig. 5(l)], bright punctuate fluorescence is also observed.

3.7 Normal Fallopian Tube Fimbria

As mentioned above, the fimbrial epithelium has been implicated as the epicenter of ovarian carcinoma development in recent studies and therefore potentially a critical region to examine for early detection. In addition to the ovarian tissues, we examined 39 tissue specimens originating from fallopian tube tissue, of which 23 were diagnosed as normal, four as normal with stripped epithelium, 11 with chronic salpingitis, and only one cancerous case of serous adenocarcinoma of the fallopian tube. Histology of normal fallopian tube [Fig. 6(a)] shows uniformly epithelialized fimbriae with clearly defined boundaries and a semiregular distribution of stromal cells arranged in a storiform pattern. VHIS imaging of the fallopian fimbria revealed a unique and consistent pattern in reflectance- and fluorescence-modes [Figs. 6(d) and 6(g), respectively] of a regular pattern similar to that observed in normal ovary, but with larger features and a deep furrowing pattern. Although specific features from VHIS images of fallopian fimbrial did not clearly correlate to histological morphology, the uniformity of the images suggest that we may actually peering onto many fimbriae slumped upon each other, a nonphysiological morphology induced by placement in the Petri dish for imaging.

3.8 Fallopian Tube Serous Adenocarcinoma

Only one cancerous abnormality involving the fallopian tube was identified in the form of fallopian tube serous adenocarcinoma, as shown by histology in Fig. 6(b). Much like serous adenocarcinoma of the ovary, this fallopian tube version is also characterized by invasive and complex papillary architecture with irregular and variable nuclei. The reflectance-mode VHIS image [Fig. 6(e)] revealed a vastly different architecture
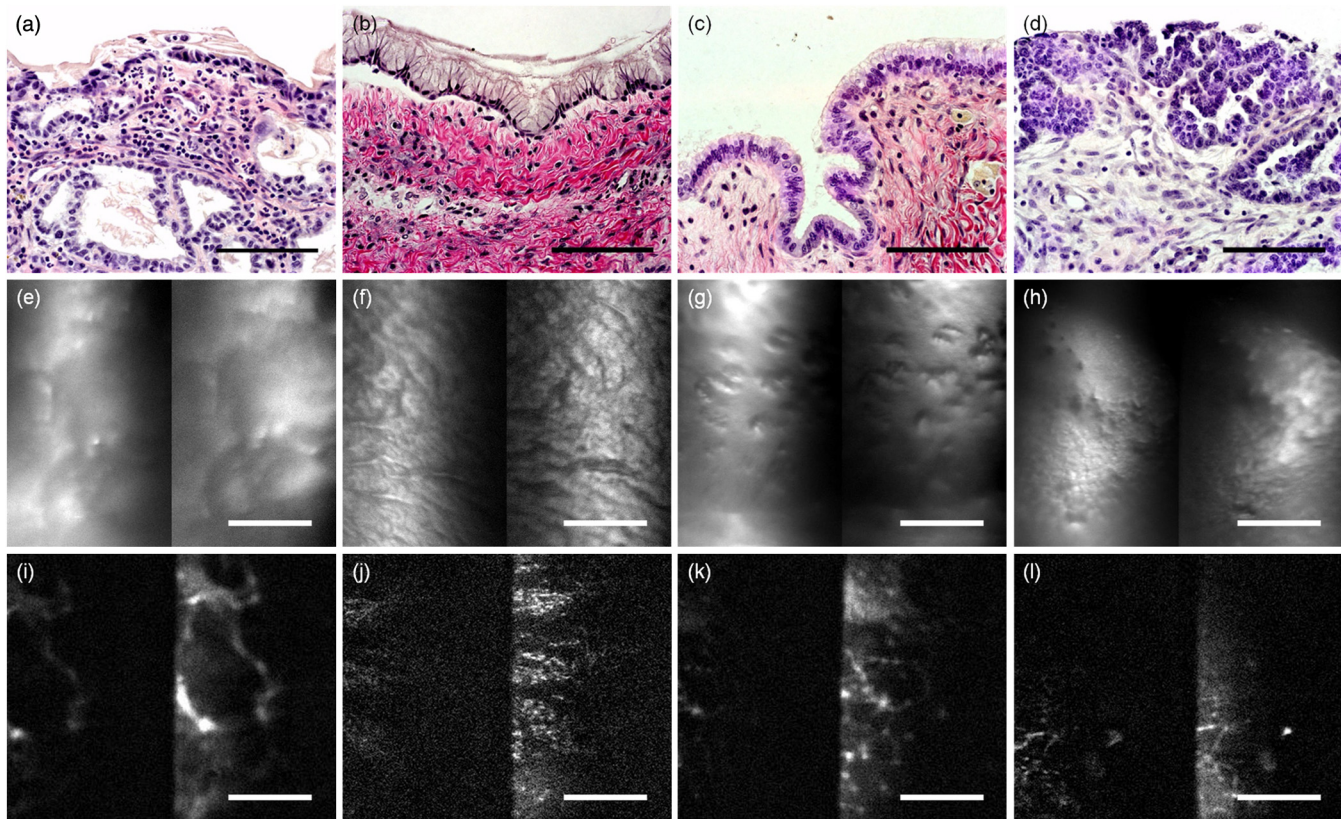
Fig. 5 Examples of abnormal ovarian tissues. This panel of images shows cross-sectional H&E-stained histology (a–d), *en face* reflectance-mode VHIS (e–h), and *en face* fluorescence-mode VHIS (i–l) images of (from left to right) mucinous adenocarcinoma, benign mucinous cystadenoma, benign serous cystadenoma, and ovarian serous adenocarcinoma metastasis to peritoneum. VHIS image orientation is orthogonal to the histology orientation. For all VHIS images, the left half is the surface image and the right half is the subsurface image. Scale bar = 100 μm, all images.

than the normal fallopian tube, with a generally smoother appearance with a small number of irregular features. Fluorescence-mode VHIS images [Fig. 6(h)] also showed some irregularity, however only a very low signal level was observed.

3.9 *Chronic Salpingitis*

Chronic salpingitis is defined as inflammation of the fallopian tube, often caused by repeated or persistent bacterial or viral infections or other constant perturbations of the fallopian tubes. This condition is characterized by blunted or fused fallopian fimbriae as seen in histology [Fig. 6(c)]. Both the reflectance- and fluorescence-mode VHIS images of chronic salpingitis [Figs. 6(f) and 6(i), respectively] show a lower frequency pattern than observed in normal fallopian tube which instead exhibits many delicate fimbriae.

4 Discussion

The results of this *ex vivo* tissue study support the development of multiplexed volume holographic imaging for imaging surface and subsurface morphologies of ovarian, tubal, and other gynecologic tissues. The VHIS implementation described here is considered for adaptation for future *in vivo* preclinical microlaparoscopic imaging of surface and subsurface features. The most striking correlation in VHIS images and tissue diagnosis was seen in both the normal ovarian tissues and ovarian serous adenocarcinoma. Normal ovarian tissue consistently showed a regular morphology under both the reflectance and fluorescent imaging modes, similar to what was observed in histology. Characteristic features included a regular cobblestone appearance in the surface image (left channel), matching the regularity of a healthy epithelium, and a regular subsurface pattern corresponding to the regularity of the stromal collagen. The regular cobblestone pattern was also observed in the fluorescence images. In ovarian serous adenocarcinoma, the *en face* VHIS images were strikingly different than the normal ovarian tissues, with an irregular topography consistent with the irregularity of carcinoma growth and micropapillae. In fluorescence-mode images, larger and irregularly shaped cells with nuclear atypia were observed, characteristic of cancerous epithelial cells. Analysis of the fallopian tube was confounded by folding of the normal fimbria and by the limited number of fallopian tube cancers (one) included in this study. Future studies will specifically include VHIS imaging of normal fallopian tube and its discrimination from serous adenocarcinoma involving the tube.

To determine the sensitivity and specificity of VHIS as a diagnostic tool for ovarian cancer, detailed examination of VHIS images, either computationally or by trained observers, will be necessary. Traditional histological analysis of tissue biopsies remains the gold standard for diagnosing ovarian cancer; however, the potential real-time information that laparoscopic VHIS provides to the oncological surgeon could help to inform *in situ* decisions to remove or preserve a patient's ovaries more rapidly than waiting for histological results. A diagnostic
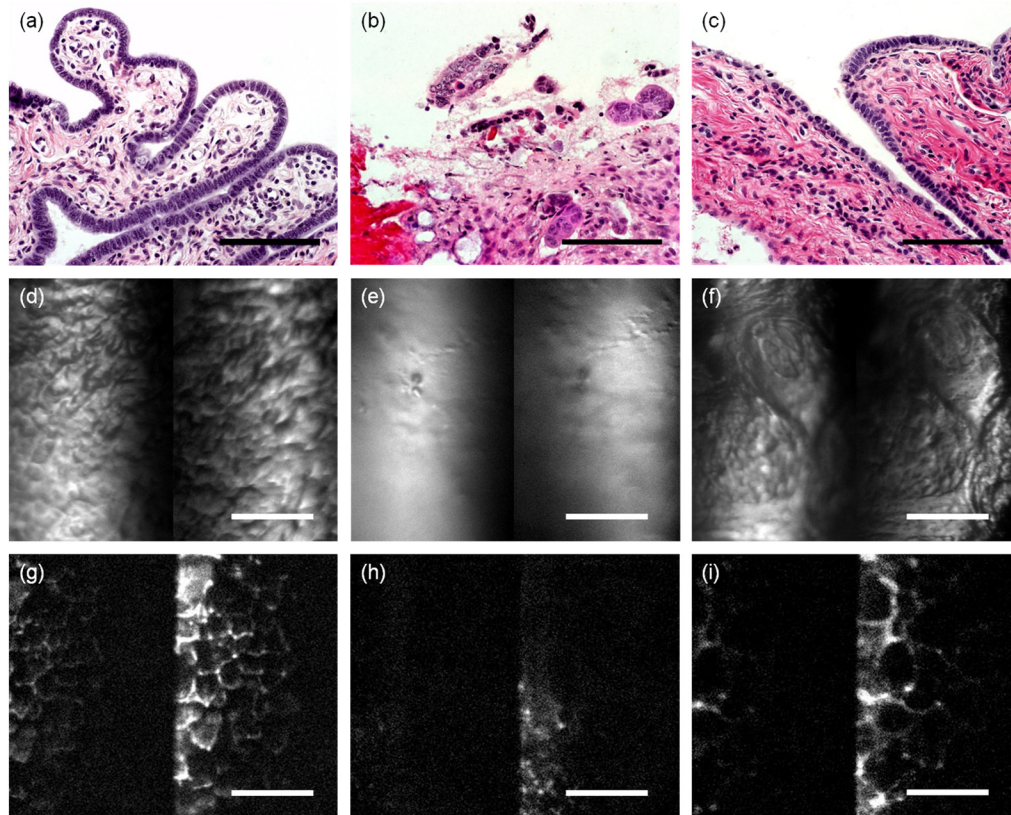
Fig. 6 Examples of normal and abnormal fallopian tube. This panel of images shows cross-sectional H&E-stained histology (a–c), *en face* reflectance-mode VHIS (d–f), and *en face* fluorescence-mode VHIS (g–i) images of (from left to right) normal fimbriated fallopian tube, fallopian tube serous adenocarcinoma, and salpingitis. VHIS image orientation is orthogonal to the histology orientation. For all VHIS images, the left half is the surface image and the right half is the subsurface image. Scale bar = 100 μm, all images.

laparoscopy with the VHIS may be useful for detecting cancer in normal-risk patients already undergoing exploratory laparotomy or laparoscopy, or for high-risk patients desiring regular laparoscopic screening with sensitive optical techniques as a short-term option to preserve fertility.

Future quantitative analysis of VHIS images will likely elucidate the diagnostic capability of VHIS. We have previously shown that a variety of quantitative image analysis techniques can be useful for identifying diseased tissues.[16,43] In particular, analysis of the spatial frequency spectrum and gray-level co-occurrence matrix parameters of OCT and SHG images has shown promise for automated, quantitative discrimination between normal and abnormal tissues. These techniques will be applied to VHIS images to assess their utility as quantitative methods discerning normal tissue from ovarian cancer.

The addition of fluorescent contrast agents to the VHIS was demonstrated using commercially available fluorescent dyes that target the cell membrane or nucleus. Although this was performed to demonstrate the ability of the system in capturing fluorescent images, future directions point toward the use of targeted contrast agents to highlight abnormal patterns of receptor expression associated with cancerous cells and tissues, as previously demonstrated *in vivo* using fluorescein loaded liposomes targeted to the folate receptor.[44,45]

With VHIS, the hologram maps spectral and spatial information along the *x*-axis, resulting in an image inherently weighted by spectral intensity distribution of light reaching the CCD camera. In the case of reflectance mode images, this distribution is determined by the spectrum of the broadband LED used for illumination which is nearly uniform, however rolls off along the edges leading to a narrowed FOV. Future versions of the VHIS will address this limitation by instead using a broader spectral band source in combination with a band-pass filter that corresponds to the spectral range observed with the hologram. For fluorescent mode imaging, the spectral–spatial mapping leads to an image that is intensity weighted by the shape of the fluorescence emission spectrum. With the fluorescent dyes used in the report, sharp emission peaks near 670 nm results in bright image features on the leftmost portion of each channel with rapid diminishing of fluorescence signal moving to the right, or long wavelengths. Unlike traditional fluorescence microscopy, where the signal represents the integral of fluorescence emission intensities within the entire spectral range captured through optical filters, VHIS fluorescence disperses the signal. To address this deficiency, alternative dyes with broader fluorescence spectra or holograms designed to disperse a narrower band of wavelengths could be added for future investigation. Alternatively, the fluorescence images could be divided by the fluorescent dye's emission spectrum along the *x*-axis to attempt to equalize the signal. To take advantage of dispersion of the fluorescence spectrum along the *x*-axis in the VHIS images, the use of specialized fluorescent dyes that exhibit spectral shifts in response to local environmental changes, such as pH or oxygenation, could reveal useful information about suspect tissues.

Channel-by-channel optical depth sectioning is important to clearly observe distinct morphological features at the surface and subsurface locations in the tissue. The hologram used in this study was fabricated with an imaging depth separation of 50 μm. The measured full width at half maximum of the axial point spread function at both of these depths was 22 μm. Upon observation of the reflectance VHIS images of gynecologic tissues, it is apparent that there is some crosstalk between channels. Work to suppress channel crosstalk is currently underway by combining highly selective volume holograms with structured illumination to increase depth selectivity.[26,46]

The image intensity that reaches the CCD camera in the VHIS is very low compared to the illumination source due to loss in the instrument optics (particularly from the 50/50 beam splitter utilized to operate in the reflectance mode, attenuation in the tissue, and selectivity of the hologram. Nearly 95% of light is not Bragg matched to the hologram (i.e., it does not correspond to the desired imaging depths) and passes through hologram and is captured by the beam dump. We estimate that the final photon flux that reaches the CCD camera is 2 to 3 orders of magnitude less than the photon flux of the illumination light. However, as demonstrated by the images shown within, the signal falls within the dynamic range and sensitivity of the camera and allows frame rates up to 20 fps.

For this benchtop trial, imaging was performed in the dark to keep background noise low and preserve signal-to-noise ratio appropriate for video-rate holographic imaging. A future adaptation of the system for use in exploratory laparotomy, a situation where turning off room lights would not be ideal, could be designed for near-infrared (NIR) illumination (above 800 nm) to avoid background contribution from ambient light. VHIS fluorescence imaging could be achieved by administering intravenous, intraperitoneal, or topical fluorescent agents that fluoresce in the NIR, such as FDA-approved indocyanine green (ICG). As we have previously demonstrated using the PQ-PMMA holographic polymer for imaging at wavelengths up to 1500 nm,[47] ICG fluorescence imaging would be compatible with VHIS.

5 Conclusion

We have demonstrated the use of VHIS for imaging *ex vivo* ovarian tissue specimens, enabling qualitative discrimination of normal and abnormal tissues as confirmed by histology. The benchtop VHIS described here provided simultaneous *en face* visualization of two image planes, at the tissue surface and at a depth of 50 μm in the tissue, expandable up to five or more imaging planes with a volume hologram constructed under different parameters. As evident in the example images shown in this paper, VHIS is capable of both epireflectance and epifluorescence imaging. We specifically designed the benchtop VHIS for rapid adaptation into an endoscopic version for an *in vivo* clinical trial, achievable by simply replacing the objective lens with a custom endoscope, and encasing the optical components and volume hologram into a handheld tool. Because VHIS is constructed in a mechanically simple and robust fashion, as it does not require raster scanning or specialized light sources to operate, rapid translation into a durable clinical instrument is feasible. We believe that widespread adoption of an optical imaging modality like VHIS for clinical visualization of early stage ovarian cancer has the potential to reduce the mortality and preserve fertility in high risk women. The results from this study assessing VHIS for simultaneous surface and subsurface imaging of gynecological tissues are promising for future clinical application of an endoscopic VHIS.

References

1. American Cancer Society, "Cancer Facts & Figures 2013," 2013, http://www.cancer.org/research/cancerfactsfigures/cancerfactsfigures/cancer-facts-figures-2013 (2 October 2013).
2. D. A. Fishman et al., "The role of ultrasound evaluation in the detection of early-stage epithelial ovarian cancer," *Am. J. Obstet. Gynecol.* **192**(4), 1214–1221 (2005).
3. D. Badgwell and R. C. Bast Jr., "Early detection of ovarian cancer," *Dis. Markers* **23**(5–6), 397–410 (2007).
4. D. L. Clarke-Pearson, "Screening for ovarian cancer," *N. Engl. J. Med.* **361**(2), 170–177 (2009).
5. Y. Lee et al., "A candidate precursor to serous carcinoma that originates in the distal fallopian tube," *J. Pathol.* **211**(1), 26–35 (2007).
6. E. Lengyel, "Ovarian cancer development and metastasis," *Am. J. Pathol.* **177**(3), 1053–1064 (2010).
7. S. Vaughan et al., "Rethinking ovarian cancer: recommendations for improving outcomes," *Nat. Rev. Cancer* **11**(10), 719–725 (2011).
8. D. Hanahan and R. A. Weinberg, "Hallmarks of cancer: the next generation," *Cell* **144**(5), 646–674 (2011).
9. Y. Chen et al., "Ultrahigh resolution optical coherence tomography of Barrett's esophagus: preliminary descriptive clinical study correlating images with histology," *Endoscopy* **39**(07), 599–605 (2007).
10. L. P. Hariri et al., "Laparoscopic optical coherence tomography imaging of human ovarian cancer," *Gynecol. Oncol.* **114**(2), 188–194 (2009).
11. L. P. Hariri et al., "Simultaneous optical coherence tomography and laser induced fluorescence imaging in rat model of ovarian carcinogenesis," *Cancer Biol. Ther.* **10**(5), 438–447 (2010).
12. A. A. Tanbakuchi et al., "In vivo imaging of ovarian tissue using a novel confocal microlaparoscope," *Am. J. Obstet. Gynecol.* **202**(90), e1–e9 (2010).
13. K. König et al., "Clinical two-photon microendoscopy," *Microsc. Res. Tech.* **70**(5), 398–402, (2007).
14. D. Granot et al., "In vivo imaging of the systemic recruitment of fibroblasts to the angiogenic rim of ovarian carcinoma tumors," *Cancer Res.* **67**(19), 9180–9189 (2007).
15. R. M. Williams et al., "Strategies for high-resolution imaging of epithelial ovarian cancer by laparoscopic nonlinear microscopy," *Transl. Oncol.* **3**(3), 181–194 (2010).
16. J. M. Watson et al., "Analysis of second-harmonic-generation microscopy in a mouse model of ovarian carcinoma," *J. Biomed. Opt.* **17**(7), 0760021 (2012).
17. J. M. Watson et al., "Two-photon excited fluorescence imaging of endogenous contrast in a mouse model of ovarian cancer," *Lasers Surg. Med.* **45**(3), 155–166 (2013).
18. U. Utzinger et al., "Reflectance spectroscopy for in vivo characterization of ovarian tissue," *Lasers Surg. Med.* **28**(1), 56–66 (2001).
19. Y. Mirabal et al., "Reflectance spectroscopy for in vivo detection of cervical precancer," *J. Biomed. Opt.* **7**(4), 587–594 (2002).

20. E. Salomatina et al., "Optical properties of normal and cancerous human skin in the visible and near-infrared spectral range," *J. Biomed. Opt.* **11**(6), 064026 (2006).
21. V. Untereiner et al., "Optical diagnosis of peritoneal metastases by infrared microscopic imaging," *Anal. Bioanal. Chem.* **393**(6–7), 1619–1627 (2009).
22. V. Krishnaswamy et al., "Quantitative imaging of scattering changes associated with epithelial proliferation, necrosis, and fibrosis in tumors using microsampling reflectance spectroscopy," *J. Biomed. Opt.* **14**(1), 014004 (2009).
23. J. Adur et al., "Quantitative changes in human epithelial cancers and osteogenesis imperfecta disease detected using nonlinear multicontrast microscopy," *J. Biomed. Opt.* **17**(8), 0814071 (2012).
24. O. Nadiarnykh et al., "Alterations of the extracellular matrix in ovarian cancer studied by second harmonic generation imaging microscopy," *BMC Cancer* **10**(1), 94 (2010).
25. G. Barbastathis and D. J. Brady, "Multidimensional tomographic imaging using volume holography," *Proc. IEEE* **87**(12), 2098–2120 (1999).
26. J. M. Castro et al., "Confocal rainbow volume holographic imaging system," *Appl. Opt.* **50**(10), 1382–1388 (2011).
27. Y. Luo et al., "Laser-induced fluorescence imaging of subsurface tissue structures with a volume holographic spatial-spectral imaging system," *Opt. Lett.* **33**(18), 2098–2100 (2008).
28. P. J. Gelsinger-Austin et al., "Optical design for a spatial-spectral volume holographic imaging system," *Opt. Eng.* **49**(4), 043001 (2010).
29. Y. Luo et al., "Optimization of multiplexed holographic gratings in PQ-PMMA for spectral-spatial imaging filters," *Opt. Lett.* **33**(6), 566–568 (2008).
30. H. Kogelnik, "Coupled wave theory for thick hologram gratings," *Bell Syst. Tech. J.* **48**(9), 2909–2947 (1969).
31. H. Lee et al., "Near-infrared pH-activatable fluorescent probes for imaging primary and metastatic breast tumors," *Bioconjug. Chem.* **22**(4), 777–784 (2011).
32. H. Kobayashi and P. I. Choyk, "Target-cancer-cell-specific activatable fluorescence imaging probes: rational design and in vivo applications," *Acc. Chem. Res.* **44**(2), 83–90 (2011).
33. J. M. Castro et al., "Analysis of diffracted image patterns from volume holographic imaging systems and applications to image processing," *Appl. Opt.* **50**(2), 170–176 (2011).
34. J. M. Castro et al., "Spatial-spectral volume holographic systems: resolution dependence on effective thickness," *Appl. Opt.* **50**(7), 1038–1046 (2011).
35. Y. Luo et al., "Silicon oxide nano-particles doped PQ-PMMA for volume holographic imaging filters," *Opt. Lett.* **35**(8), 1269–1271 (2010).
36. Y. Luo et al., "Simulations and experiments of aperiodic and multiplexed gratings in volume holographic imaging systems," *Opt. Express* **18**(18), 19273–19285 (2010).
37. D. Psaltis and G. Barbastathis, "Real-time spectral imaging in three spatial dimensions," *Opt. Lett.* **27**(10), 854–856 (2002).
38. W. Liu et al., "Volume holographic hyperspectral imaging," *Appl. Opt.* **43**(18), 3581–3599 (2004).
39. Y. Luo et al., "Wavelength-coded multifocal microscopy," *Opt. Lett.* **35**(5), 781–783 (2010).
40. Y. Luo et al., "Phase-contrast volume holographic imaging system," *Opt. Lett.* **36**(7), 1290–1292 (2011).
41. F. Medeiros et al., "The tubal fimbria is a preferred site for early adenocarcinoma in women with familial ovarian cancer syndrome," *Am. J. Surg. Pathol.* **30**(2), 230–236 (2006).
42. J. Kim et al., "High-grade serous ovarian cancer arises from fallopian tube in a mouse model," *Proc. Natl. Acad. Sci. U. S. A.* **109**(10), 3921–3926 (2012)..
43. K. W. Gossage et al., "Texture analysis of optical coherence tomography images: feasibility for tissue classification," *J. Biomed. Opt.* **8**(3), 570–575 (2003).
44. G. M. van Dam et al., "Intraoperative tumor-specific fluorescence imaging in ovarian cancer by folate receptor-α targeting: first in-human results," *Nat. Med.* **17**(10), 1315–1319 (2011).
45. M. J. Turk, D. J. Waters, and P. S. Low, "Folate-conjugated liposomes preferentially target macrophages associated with ovarian carcinoma," *Cancer Lett.* **213**(2), 165–172 (2004).
46. E. E. de Leon et al., "Dual-grating confocal-rainbow volume holographic imaging system designs for high depth resolution," *Appl. Opt.* **51**(29), 6952–6961 (2012).
47. A. Sato and R. K. Kostuk, "Holographic grating for dense wavelength division optical filters at 1550 nm using phenanthrenquinone-doped poly (methyl methacrylate)," *Proc. SPIE* **5216**, 44–52 (2003).

Biographies of the authors are not available.